nature materials

ARTICLES

https://doi.org/10.1038/s41563-019-0485-2

Collective topo-epitaxy in the self-assembly of a 3D quantum dot superlattice

Alex Abelson[1,6], Caroline Qian[2,6], Trenton Salk[3], Zhongyue Luan[1], Kan Fu[1], Jian-Guo Zheng[4], Jenna L. Wardini[1] and Matt Law[1,2,5*]

Epitaxially fused colloidal quantum dot (QD) superlattices (epi-SLs) may enable a new class of semiconductors that combine the size-tunable photophysics of QDs with bulk-like electronic performance, but progress is hindered by a poor understanding of epi-SL formation and surface chemistry. Here we use X-ray scattering and correlative electron imaging and diffraction of individual SL grains to determine the formation mechanism of three-dimensional PbSe QD epi-SL films. We show that the epi-SL forms from a rhombohedrally distorted body centred cubic parent SL via a phase transition in which the QDs translate with minimal rotation (~10°) and epitaxially fuse across their {100} facets in three dimensions. This collective epitaxial transformation is atomically topotactic across the 10^3–10^5 QDs in each SL grain. Infilling the epi-SLs with alumina by atomic layer deposition greatly changes their electrical properties without affecting the superlattice structure. Our work establishes the formation mechanism of three-dimensional QD epi-SLs and illustrates the critical importance of surface chemistry to charge transport in these materials.

A major challenge in mesoscience is to achieve the delocalization of electronic wavefunctions and the formation of bulk-like electronic bands ('minibands') in assemblies of nanoscale building blocks. Colloidal semiconductor quantum dots (QDs) are well-defined, novel and versatile building blocks whose interactions in self-assembled solids are highly tunable, which makes QD solids an exciting playground for mesoscale science[1]. Theoretical calculations predict that miniband formation in highly ordered, highly coupled QD superlattices (SLs) (crystals of QDs) can boost charge carrier mobility and diffusion length[2–5], which might enable a new class of designer QD solids that combines bulk-like electronic performance with the unique photophysics and solution processability of colloidal QDs. However, the relatively high energetic and spatial disorder of all the colloidal QD solids studied to date inhibit the emergence of new collective mesoscale behaviour and result, instead, in weakly coupled QD films with unremarkable properties[4,6–9].

Several groups recently pioneered the fabrication of highly ordered PbX (X = S, Se) QD SLs in which the QDs are epitaxially interconnected to form porous single crystals[10,11]. Typically made by self-assembly on a liquid surface[12,13], these 'confined-but-connected' epitaxially fused QD SLs (epi-SLs) feature exceptional coupling and spatial order and are promising systems for miniband formation. Most reports focus on two-dimensional (2D) epi-SLs (QD monolayers) due to their anticipated exotic band structures and relatively simple fabrication and characterization[4,9–11,14–22]. 3D epi-SLs have received much less attention[11,23–25]. Transport measurements of 2D epi-SLs show that multiple sources of disorder (such as variation in the number, width and atomic perfection of epitaxial connections) prevent significant carrier delocalization despite strong inter-QD coupling[4,9,21]. To provide a basis for rationally improving the spatial and energetic order of epi-SLs, it is essential to establish the mechanism(s) by which epi-SLs form. Researchers have studied the formation of 2D epi-SLs by in situ X-ray scattering[17] and presented a conceptual formation mechanism for 3D epi-SLs[24], but a basic structural–chemical understanding of the phase transition is far from complete, particularly for 3D films.

Here we establish the formation mechanism of a 3D PbSe QD epi-SL based on a thorough understanding of the structures of the parent and product phases. We show that the epi-SL forms from a rhombohedrally distorted body-centred cubic (bcc) unit cell in which each QD is surrounded by six nearest neighbours rotationally aligned with cofacial {100} facets. The phase transition occurs by a nearly pure translational motion of the QDs (10° rotation), followed by epitaxial fusion of their {100} facets in three dimensions. This phase transition combines collective 3D epitaxy with atomic topotaxy, which means that the atomic lattices (ALs) of the two SLs have a specific 3D crystallographic relationship[26]. Unlike classic examples of topotaxy, such as cation exchange[27], intercalation[28] and the conversion of sapphire into spinel[29], the formation of the epi-SL is a collective topotactic transformation of an entire ensemble of crystals (10^3–10^5 QDs per SL grain).

We fabricated epi-SLs using oleate-capped colloidal PbSe QDs with a diameter of 6.5 ± 0.3 nm and a first exciton energy of 0.675 eV (Methods and Supplementary Fig. 1). Single-particle reconstruction of scanning transmission electron microscopy (STEM) images revealed that these QDs are non-uniform truncated cuboctahedra with six {100}, twelve {110} and eight {111} facets (accounting for 33%, 27% and 40%, respectively, of the total QD surface area of 145 nm^2) (ref. [30]). Quantitative NMR spectroscopy showed that there are 505 ± 28 oleate ligands per QD (3.48 oleate nm^{-2} (Supplementary Method 1)). Based on the calculated binding energies of oleate on PbSe surfaces[31], we estimated oleate coverages of 3.7–5.0, 2.0–4.3 and 0–1.0 nm^{-2} on the {111}, {110} and {100} facets, respectively (Supplementary Fig. 2). We therefore believe that these QDs have patchy ligand coverage and nearly bare {100} facets.

[1]Department of Materials Science and Engineering, University of California, Irvine, Irvine, CA, USA. [2]Department of Chemical and Biomolecular Engineering, University of California, Irvine, Irvine, CA, USA. [3]Department of Physics and Astronomy, University of California, Irvine, Irvine, CA, USA. [4]Irvine Materials Research Institute, University of California, Irvine, Irvine, CA, USA. [5]Department of Chemistry, University of California, Irvine, Irvine, CA, USA. [6]These authors contributed equally: Alex Abelson, Caroline Qian. *e-mail: matt.law@uci.edu

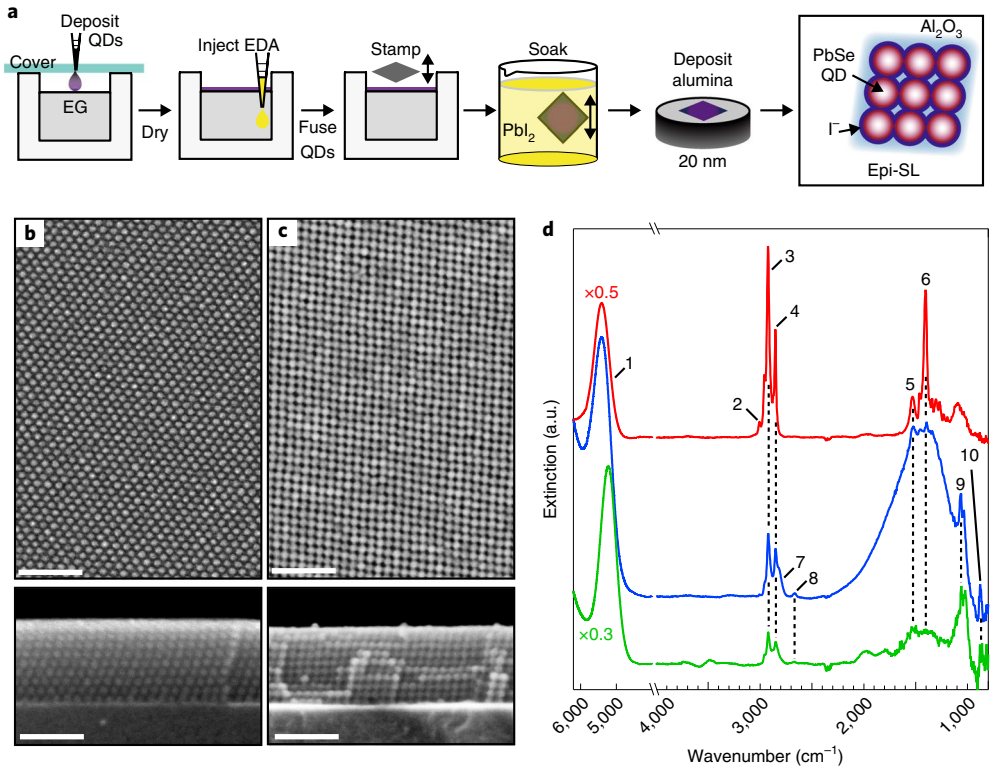

Fig. 1 | Fabrication and ligand chemistry of PbSe QD epi-SLs. a, Process flow for the fabrication of ALD-infilled PbSe QD epi-SLs. **b**, Plan view (top) and cross-sectional (bottom) SEM images of a typical oleate-capped SL film on a silicon substrate. The images show a $(101)_{SL}$-oriented grain that is ten QDs thick. Scale bar, 50 nm. **c**, Corresponding SEM images of an epi-SL after EDA and PbI_2 treatment (no ALD). The images show a $(100)_{SL}$-oriented grain, also ten QDs thick. Scale bar, 50 nm. **d**, FTIR spectra of an oleate-capped SL (red) and epi-SL before (blue) and after (green) the PbI_2 treatment. Labelled peaks are assigned as follows: peak 1 is the first exciton transition of the QDs, peaks 2–6 are adsorbed oleate (2, ν(HC=CH); 3, $\nu_{as}(CH_2)$; 4, $\nu_s(CH_2)$; 5, $\nu_{as}(COO^-)$; 6, $\nu_s(COO^-)$) and peaks 7–10 are adsorbed ethylene glycoxide (7, $\nu_{as}(CH_2)$; 8, $\nu_s(CH_2)$; 9, ν(CO) and ν(CC); 10, $\rho(CH_2$ rocking)). All the films have the same number of QD layers and are 50–60 nm thick. Spectra are baseline corrected using a spline fit and offset. The oleate-capped SL spectrum is scaled by ×0.5 and the exciton region of the PbI_2-treated epi-SL is scaled by ×0.3. Supplementary Fig. 3 gives the raw spectra and Supplementary Fig. 4 gives additional analysis of the SL ligand chemistry. a.u., arbitrary units.

Figure 1a shows the fabrication process used to make the epi-SLs discussed in this article. First, oleate-capped QD SL films were formed by self-assembly from a hexane suspension on the surface of liquid ethylene glycol (EG)[12,13]. Controlled evaporation of the hexane resulted in polycrystalline SL films with a thickness of 50–80 nm and an average lateral grain size of ~500 nm (Fig. 1b). Next, a solution of 1,2-ethylenediamine (EDA) was injected into the EG to trigger epitaxial fusion of the QDs across their {100} facets by removing oleate ligands and enabling a direct QD–QD contact[4]. The ligand exchange and epitaxial fusion started at the bottom of the floating QD film and propagated upward to the top surface of the film. We believe that the polar EG solution wicks into the film as oleate is replaced with glycoxide during the ligand exchange process (see below), ultimately to yield epi-SLs with a uniform QD fusion and ligand coverage for films thin enough to avoid a significant exchange gradient (<250 nm). The epi-SLs were then stamp transferred to a solid substrate and immersed in a solution of PbI_2 with the goal to remove residual ligands and produce an all-inorganic SL with improved environmental stability and charge transport[32]. The resulting films were polycrystalline epi-SLs with an average lateral grain size of ~250 nm and significant nanoscale cracking (Fig. 1c). Finally, these epi-SLs were infilled and overcoated with amorphous alumina using low-temperature atomic layer deposition (ALD), previously shown to enhance the environmental stability and carrier mobilities of amorphous QD films[7].

The ligand content of the SLs is important because surface chemistry usually dictates the electronic properties of QD films[8,33,34]. Fourier transform infrared (FTIR) spectra showed that the EDA treatment removed ~88% of the oleate C–H signal intensity and added a large amount of adsorbed ethylene glycoxide to the epi-SL (Fig. 1d). Unfortunately, the glycoxide surface coverage could not be reliably quantified from these data. No evidence for adsorbed EDA was found by FTIR spectroscopy or X-ray photoelectron spectroscopy (Supplementary Fig. 5). These results were corroborated by FTIR spectra of films treated with deuterated EG and EDA (Supplementary Fig. 4) and are consistent with reports that amines do not readily adsorb to PbSe QDs[35]. Furthermore, we found by inductively coupled plasma mass spectroscopy (ICP-MS) that the EDA treatment stripped a small number of Pb but no Se atoms from the QDs (Supplementary Method 2)[36]. The subsequent PbI_2 treatment removed another 6% of the original oleate and ~80% of the glycoxide signal (Fig. 1d) and coated the SL in a submonolayer of adsorbed iodide (Supplementary Fig. 5). The PbI_2-treated epi-SLs therefore had a mixture of oleate (~6% of the original amount), glycoxide and iodide/PbI_2 ligands. More extreme EDA treatments caused excessive QD fusion and amorphization of the SLs, whereas more-extreme PbI_2 treatments resulted in no additional fusion or ligand removal (Supplementary Fig. 6). As only EDA causes QD fusion, EDA followed by PbI_2 is a useful dual-treatment approach to independently tune the degree of QD fusion and the organic ligand coverage of these epi-SLs.

We determined the unit cells of both the oleate-capped and epi-fused SLs with an accuracy of ~1 Å and ~1° using a combination of synchrotron grazing-incidence small-angle X-ray scattering

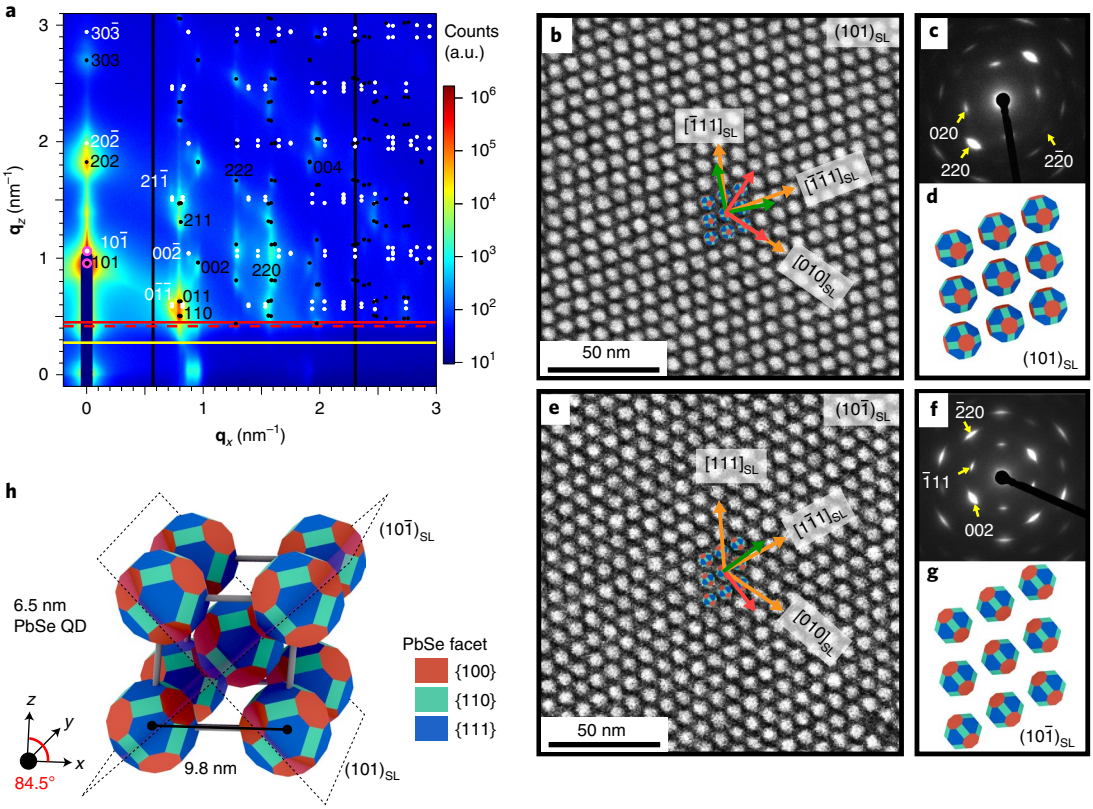

Fig. 2 | Structure of the oleate-capped QD SL films. a, A 2D GISAXS pattern of a typical film on a silicon substrate. Overlaid is the calculated spot pattern for a body-centred unit cell ($a=c=9.78$ nm, $b=9.8$ nm, $\alpha=85.5°$, $\beta=84.5°$, $\gamma=84°$) oriented with a mixture of its (101) and (10$\bar{1}$) planes parallel to the substrate surface (black and white dots, respectively). For clarity, only select Miller indices are labelled. The solid and dashed red lines denote the scattering vector $\mathbf{q}_z$, which corresponds to the critical angle of the QD film (0.195°, fit experimentally) and Si substrate (0.180°). The yellow line denotes the substrate horizon. **b**–**d**, Correlative TEM imaging and electron diffraction of a single $(101)_{SL}$-oriented SL grain. **b**, Secondary electron image of the grain. Overlaid is a model of the top monolayer of the QDs according to the lattice parameters in **h**. The orange arrows denote the crystallographic directions of the SL, and the green and red arrows indicate two of the $<100>_{AL}$ and $<110>_{AL}$ directions of the PbSe AL. **c**, Corresponding SAED pattern of the AL, with several spots labelled. The zone axis is ~15° from $[001]_{AL}$. **d**, Model of the first monolayer of QDs on this SL plane. The red, cyan and blue facets correspond to the {100}, {110} and {111} planes of PbSe. A slight tilting of the $[001]_{AL}$ from the plane normal is visible. **e**–**g**, Correlative TEM imaging and diffraction of a $(10\bar{1})_{SL}$-oriented SL grain. **e**, Secondary electron image with overlaid model and crystallographic axes. The orange arrows denote the crystallographic directions of the SL, and the green and red arrow indicate one of the $<100>_{AL}$ and $<110>_{AL}$ directions of the PbSe AL. **f**, Corresponding SAED pattern. The zone axis is $[110]_{AL}$. **g**, Model of the first monolayer of QDs on this SL plane. **h**, The average rhombohedrally distorted bcc unit cell of the oleate-capped QD SLs ($a=9.8$ nm, $\alpha=84.5°$). The $(101)_{SL}$ and $(10\bar{1})_{SL}$ planes are outlined with dashed boxes. Supplementary Fig. 9 shows wide-area SEM images of these films and Supplementary Fig. 10 gives the relationship between the conventional and primitive cells of this SL.

(GISAXS) of entire films and scanning electron microscopy (SEM) and correlated transmission electron microscopy (TEM)-based secondary electron imaging (SEI) and electron diffraction of individual SL grains. This rigorous dual-space analysis, summarized in Supplementary Fig. 7, was key to determining the complete SL unit cells and phase transformation pathway. Figure 2 shows the results for the oleate-capped SLs. These films produced strong GISAXS spot patterns characteristic of highly ordered polycrystalline thin-film SLs with a high degree of uniaxial (out-of-plane) crystallographic texture (Fig. 2a). All the patterns indexed to a body-centred unit cell with lattice parameters $a\approx b\approx c=9.8\pm0.2$ nm and $\alpha\approx\beta\approx\gamma=84.5\pm3°$. Although each individual film is triclinic, on average the oleate-capped SLs can be described with a rhombohedrally distorted body centred cubic ('distorted bcc') conventional cell ($a=9.8$ nm, $\alpha=84.5°$). The distorted bcc description is non-Bravais but easy to visualize and compare with previously published QD SLs[37,38]. GISAXS showed that the films contained SL grains of two different in-plane orientations, $(101)_{SL}$ and $(10\bar{1})_{SL}$. These SL planes are inequivalent and have distinct arrangements of QDs (Fig. 2b,e), which facilitated the use of SEM imaging to validate and refine the GISAXS fits (Supplementary Fig. 8). We found excellent agreement between the GISAXS and SEM data, which is strong evidence that the SL unit cell presented in Fig. 2 is correct. This agreement also indicates that the SL surfaces have little tendency to reconstruct, such that the SL surface and bulk share the same unit cell.

The GISAXS/SEM analysis provides the positions but not the rotational orientation of the QDs that are needed to fully specify the unit cell of the oleate-capped SL. We used TEM-based SEI and selected area electron diffraction (SAED) of individual $(101)_{SL}$- and $(10\bar{1})_{SL}$-oriented grains to determine the orientation of the QDs with respect to the SL. The images (Fig. 2b,e) provide the local SL orientation and the SAED patterns of the same grains (Fig. 2c,f) provide the relationship between the PbSe AL and QD SL. We found strong single-crystalline SAED spot patterns, which indicate that the QDs are rotationally aligned in three dimensions, with a complete biaxial alignment between the AL and SL. The crystallographic relationship deduced from correlated imaging and diffraction of many $(101)_{SL}$- and $(10\bar{1})_{SL}$-oriented grains is $(110)_{AL}||(10\bar{1})_{SL}$ and $[100]_{AL}||\angle\ 11°[1\bar{1}1]_{SL}$ (there is an 11° angle between the two directions). We conclude that the two grain orientations are simply

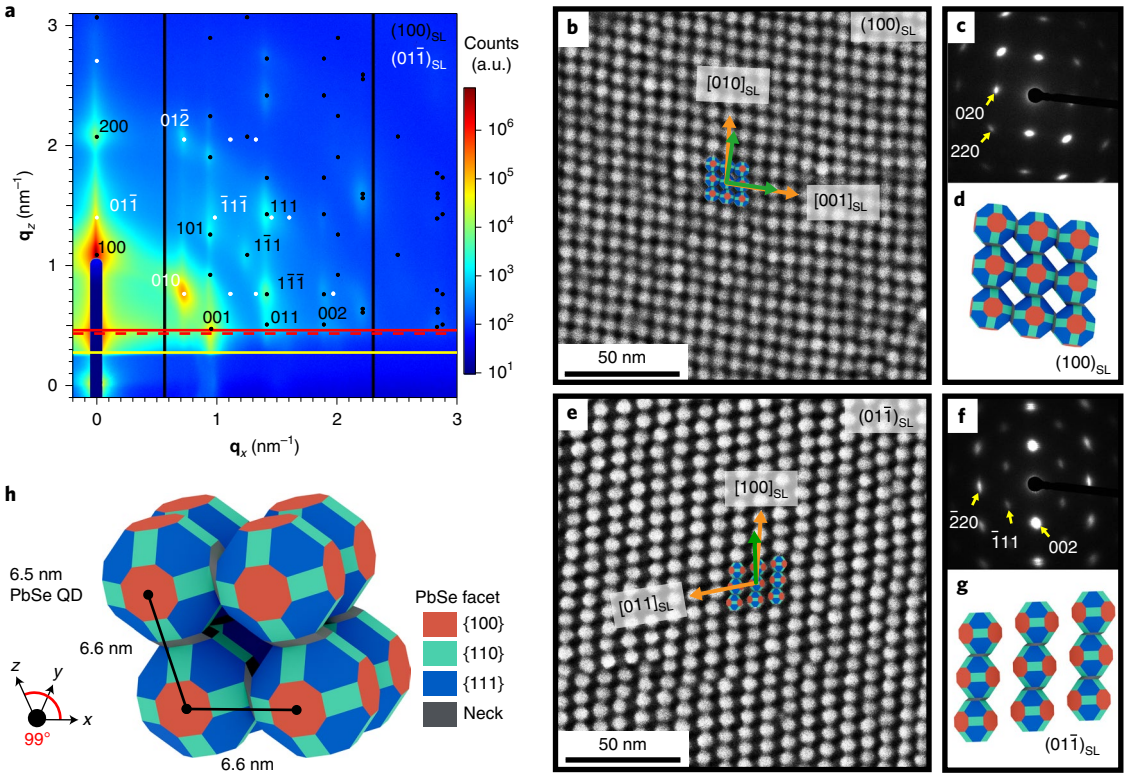

Fig. 3 | Structure of the epi-SL films. a, A 2D GISAXS pattern of a typical film on a silicon substrate. Overlaid are the calculated spot patterns for two very similar triclinic unit cells, one (black dots) with a $(100)_{SL}$ in-plane orientation ($a=6.5$ nm, $b=c=6.7$ nm, $\alpha=97°$, $\beta=\gamma=99°$) and the other (white dots) with a $(01\bar{1})_{SL}$ in-plane orientation ($a=b=c=6.5$ nm, $\alpha=95°$, $\beta=\gamma=97°$). We often observed slightly different lattice parameters for the two grain orientations. Only select Miller indices are labelled. The solid and dashed red lines denote the scattering vector $\mathbf{q}_z$ and correspond to the critical angle of the QD film (0.21°) and Si substrate (0.180°). The yellow line denotes the substrate horizon. **b**–**d**, Correlative TEM imaging and electron diffraction for a single $(100)_{SL}$-oriented grain. **b**, Secondary electron image of the $(100)_{SL}$-oriented SL grain. Overlaid is a model of the top monolayer of QDs according to the lattice parameters in **h**. The orange arrows denote the crystallographic directions of the SL, and the green arrows indicate two of the $<100>_{AL}$ directions of the PbSe AL. **c**, Corresponding SAED pattern of the AL, with several spots labelled. The zone axis is normal to $(100)_{SL}$ and ~5° from $[001]_{AL}$. **d**, Model of the first monolayer of QDs on this SL plane. The facet colours correspond to those in **h**. **e**–**g**, Correlative TEM imaging and diffraction for a $(01\bar{1})_{SL}$-oriented grain. **e**, Secondary electron image with overlaid model and crystallographic axes. The orange arrows denote the crystallographic directions of the SL, and the green arrow indicates one of the $<100>_{AL}$ directions of the PbSe AL. **f**, SAED pattern. The zone axis is $[\bar{1}\,\bar{1}0]_{AL}$. **g**, Model of the first monolayer of QDs on this SL plane. The facet colours correspond to those in **h**. **h**, The distorted simple cubic unit cell of the epi-SL ($a=6.6$ nm and $\alpha=99°$). Supplementary Fig. 15 shows wide-area SEM images of these films and Supplementary Fig. 16 gives an analysis of twinned epi-SL grains.

two views of the same structure, rather than two different unit cells. The resulting models of the $(101)_{SL}$ and $(10\bar{1})_{SL}$ surfaces are shown in Fig. 2d,g, and Fig. 2h shows the oleate-capped SL unit cell (with ligands omitted for clarity).

The distorted bcc unit cell of the oleate-capped SL is extraordinary because the QDs are prepositioned to fuse across their {100} facets by a simple translational motion. Many articles report oleate-capped PbS/Se QD SLs with cubic or tetragonal (bcc, face-centred cubic or body-centred tetragonal) unit cells and cofacial {111} facets[11,37–44], but these structures have eight or twelve nearest neighbours and require significant rotational and translational rearrangement of the QDs to form simple cubic epi-SLs[24]. In contrast, each QD in our oleate-capped SL has six nearest neighbours with cofacial {100} facets arranged in a rhombohedrally distorted octahedron (Fig. 2h and Fig. 4a). The nearest neighbours have a centre-to-centre distance of 8.2 nm and a facet-to-facet distance of 2.1 nm, comparable to the length of the oleate ligands. The QDs are prearranged to fuse to their six nearest neighbours via their six {100} facets. On the $(101)_{SL}$ plane, each QD has four close nearest neighbours with cofacial {100} facets at 8.2 nm and two far nearest neighbours with cofacial {110} facets at 9.8 nm (Fig. 2d and Supplementary Fig. 11). The QDs on this plane are arranged to fuse with their four close nearest neighbours to make a 2D quasi-square epi-SL. In contrast, each QD on the $(10\bar{1})_{SL}$ plane has two close nearest neighbours with cofacial {100} facets at 8.2 nm and four far nearest neighbours with cofacial {111} facets (two at 9.3 nm and two at 9.8 nm) (Fig. 2g and Supplementary Fig. 11). The QDs on the $(10\bar{1})_{SL}$ plane are arranged to fuse with their two close nearest neighbours to make parallel 1D chains of epi-fused QDs. Therefore, we expected the two grain orientations of the oleate-capped SL to yield two orientations of the epi-SL with very different topologies in SEM images.

The unit cell of the epi-SL films was determined in the same fashion. GISAXS/SEM analysis showed that the films were polycrystalline SLs with a triclinic primitive unit cell with lattice parameters $a\approx b\approx c=6.6\pm0.2$ nm and $\alpha\approx\beta\approx\gamma=99\pm2°$ and a mixture of $(100)_{SL}$ and $(01\bar{1})_{SL}$ in-plane grain orientations (Fig. 3a). The average structure can be described as a slightly distorted simple cubic primitive cell or a highly distorted bcc conventional cell (Fig. 4). We use the distorted simple cubic description because it is easier to visualize. As in the oleate-capped SL, each QD in the epi-SL has six nearest neighbours arranged in a rhombohedrally distorted octahedron, but with a much smaller centre-to-centre distance (6.5–6.7 nm versus 8.2 nm) because the QDs in the epi-SL are fused with epitaxial necks 1–3 atomic layers in length. Recent TEM stud-

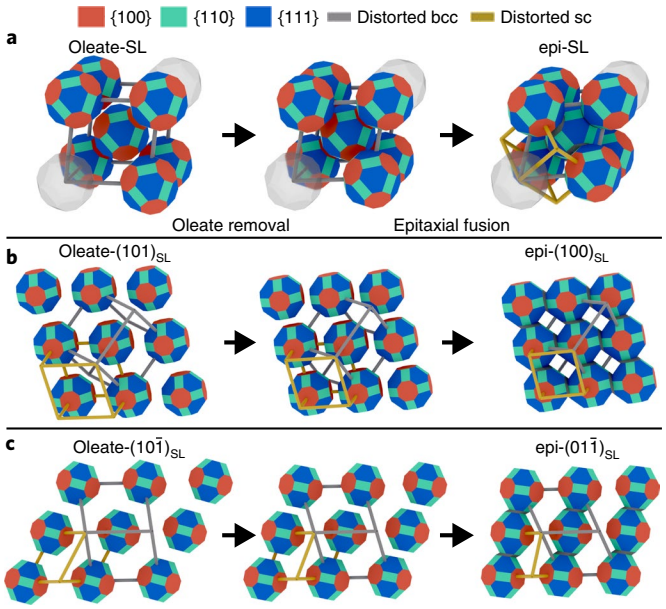

Fig. 4 | The phase transition pathway. The formation of the epi-SL proceeds by nearly pure translational motion of the QDs. **a**, Transformation of the unit cell. The distorted bcc unit cell of the oleate-capped SL (left) emphasizes the distorted octahedral, $\{100\}_{AL}$-cofacial coordination environment of each QD (left). As oleate is removed (centre), there occurs a ~1.6 nm translation of the corner QDs towards the centre QD and a slight rotation (10°) of all of the QDs about a common $[110]_{AL}$ axis (in-plane for the $(100)_{SL}$-oriented grains and out-of-plane for the $(01\bar{1})_{SL}$-oriented grains) to form the epi-SL (right). Pb and Se atoms flow into the interfacet regions to form epitaxial necks that are 0.5–1 unit cells long. The grey and yellow unit cells correspond to the distorted bcc conventional cell and distorted simple cubic primitive cell, respectively. The red, cyan and blue facets correspond to the {100}, {110} and {111} planes of PbSe. The dark grey shading denotes the epitaxial necks between QDs. **b**, Transformation of the $(101)_{SL}$ surface of the oleate-capped SL to the $(100)_{SL}$ surface of the epi-SL (key as for **a**). **c**, Transformation of the $(10\bar{1})_{SL}$ surface of the oleate-capped SL to the $(01\bar{1})_{SL}$ surface of the epi-SL (key as for **a**).

ies demonstrated that Pb and Se atoms flow from adjoining facets into the neck regions during the epitaxial fusion of PbSe QDs, and thereby distort the QD shape[30]. TEM and X-ray diffraction data show that the QDs are, indeed, epitaxially fused across their {100} facets to form a porous single-crystalline SL (Supplementary Figs. 12–14), similar to the structures reported by others[4,14,17,21]. Examples of $(100)_{SL}$- and $(01\bar{1})_{SL}$-oriented grains are shown in Fig. 3b–d and Fig. 3e–g, respectively. The $(100)_{SL}$ grains appear in secondary electron images as quasi-square 2D lattices, whereas the $(01\bar{1})_{SL}$ grains feature parallel chains of fused QDs (Fig. 3b,e). The latter morphology is expected for a {110} projection of a simple cubic lattice in which the inter-QD distance is a within the chains and $a\sqrt{2}$ between the chains. The AL and SL are crystallographically related as $(110)_{AL}||(01\bar{1})_{SL}$ and $[100]_{AL}||\angle$ 5°$[100]_{SL}$. Figure 3h depicts the average epi-SL unit cell (ligands omitted).

Figure 4 and Supplementary Video 1 show the proposed pathway of the phase transition from the oleate-capped SL to the epi-SL. The phase transition is triggered by the removal of oleate and driven by the lower surface area and free energy of the epi-fused SL. As the QDs in the oleate-capped SL are biaxially aligned with cofacial {100} facets, the formation of the epi-SL requires only translation and a 10° rotation of each QD about a common $[110]_{AL}$ axis. The coordination polyhedron of the SL (the rhombohedrally distorted octahedron (Fig. 4a)) is conserved during this phase transition and, although we emphasize the different unit cells before and after epitaxial fusion, the topology of the QD array remains fundamentally unchanged. We find that the $(101)_{SL}$- and $(10\bar{1})_{SL}$-oriented grains of the oleate-capped SL convert into $(100)_{SL}$- and $(01\bar{1})_{SL}$-oriented grains of the epi-SL, respectively, as discussed above and shown in Fig. 4b,c. 3D epi-SL formation is possible only because the void spaces between the QDs in the epi-SL unit cell are big enough to allow in-diffusion of EG and EDA and out-diffusion of oleate species from deep within the films (Supplementary Fig. 17).

This phase transition is a striking example of collective, multiscale topotaxy and epitaxy in a colloidal nanocrystal solid. The formation of the epi-SL involves a 3D epitaxial attachment of the 10^3–10^5 QDs in each SL grain. The parent and product SLs are single crystals (in both the AL and SL) related by a specific geometric transformation. Thus, the SLs have a definite 3D crystallographic relationship and the phase transition is atomically topotactic. The topotactic relationship between the SLs is $(10\bar{1})_{oleate\text{-}SL}||(01\bar{1})_{epi\text{-}SL}$ and $[1\bar{1}1]_{oleate\text{-}SL}||\angle 15.5°[100]_{epi\text{-}SL}$. Knowing that the mechanism is topotactic will help researchers improve the spatial order of these epi-SLs by optimizing the structure of the oleate-capped SLs and controlling the kinetics of the phase transition.

Given the topotactic phase transition, it is especially important to understand why the oleate-capped QDs adopt a distorted bcc unit cell with cofacial {100} facets. Several studies emphasize that the SL unit cell is determined by the effective QD shape, which is a convolution of QD faceting and ligand coverage[37,39,45]. Shape anisotropy drives orientational ordering of the QDs, which in turn determines the SL symmetry. In the present case, we speculate that there is a steric and/or electrostatic driving force for a cofacial alignment of the {100} QD facets. If cofacial {100} facet alignment lowers the SL energy, then a rhombohedral distortion from a perfect bcc unit cell is expected because such a distortion increases the {100} facet overlap (Supplementary Fig. 18). A perfect bcc cell (lattice angle $\alpha = 90°$) provides very poor {100} facet overlap (an extremely distorted octahedral coordination with the six nearest neighbours having the best {100} facet alignment). In the opposite limit of extreme rhombohedral distortion ($\alpha = 60°$), the SL has a simple cubic unit cell with perfect octahedral coordination and the maximum {100} facet overlap between the QDs (at least seven times a greater overlap area than that for bcc). We reasoned that a lower oleate coverage should increase the driving force for {100} facet overlap and result in more distorted SLs. Indeed, we found that the rhombohedral distortion systematically increased from $\alpha = 85.0°$ to $\alpha = 82.0°$ with decreasing oleate coverage (Supplementary Fig. 19). A preference for cofacial {100} facets explains the observed rhombohedral distortion and the increasing distortion with decreasing ligand coverage. Control of the rhombohedral distortion has practical importance because oleate-capped SLs with more {100} facet overlap are better positioned for fusion and may produce epi-SLs of greater structural perfection.

Finally, we assessed the structural and electronic impact of infilling and overcoating the epi-SLs with amorphous alumina by ALD. Previous work has shown that ALD infilling can greatly improve the electrical properties and environmental stability of QD solids[7,46]. We expected this approach to also be useful to tune the surface chemistry and doping of the epi-SLs. X-ray diffraction and GISAXS data showed that ALD infilling leaves the QD size, unit cell and spatial order of the epi-SLs unchanged (Supplementary Figs. 20 and 21). Cross-sectional elemental mapping of single SL grains by STEM-based energy dispersive spectroscopy (EDS) showed that the alumina infilling is uniform (Fig. 5a,b). However, infilling also caused a nearly complete bleach of the first exciton peak and the appearance of a 1S–1P intraband transition in optical absorption spectra, consistent with very strong doping of the epi-SLs by the ALD coating (Fig. 5c)[47,48]. Field-effect transistor (FET) electrical measurements corroborated these changes in the optical spectra. Before ALD, the epi-SLs acted as ambipolar transistors with dominant p channels and

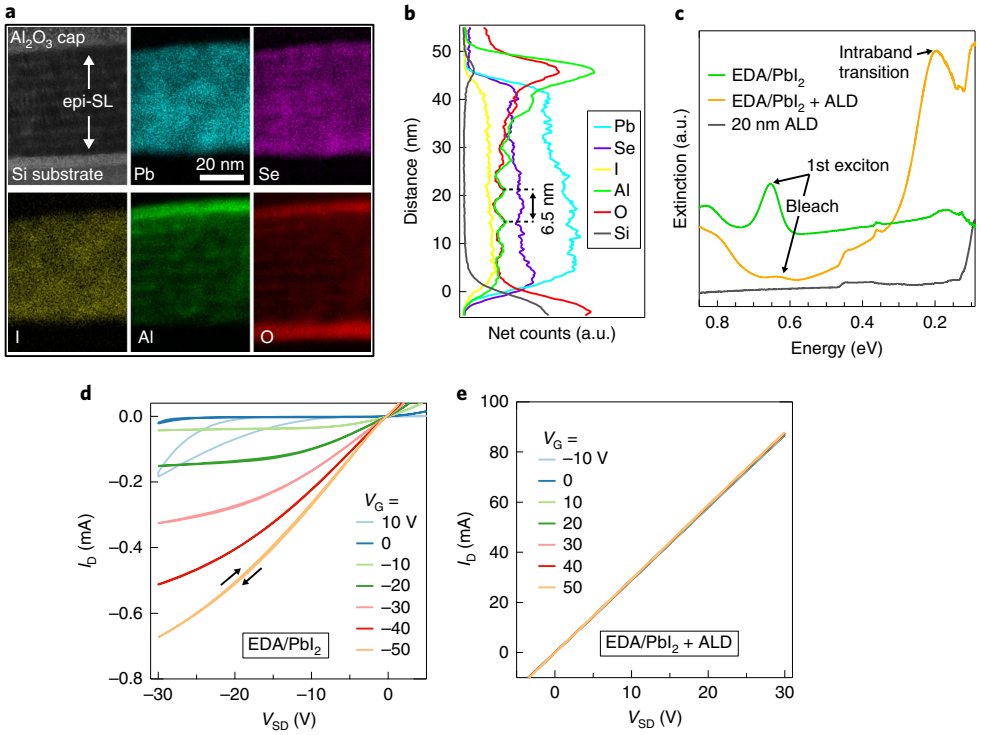

Fig. 5 | Effect of ALD alumina infilling on the epi-SLs. a, Bright-field STEM image (top left) and EDS elemental maps of a cross-section of a 51 nm thick (eight QD layers), $(100)_{SL}$-oriented, alumina-infilled epi-SL prepared on a Si substrate by a focused ion beam. **b**, The integrated line profiles of each element along the film normal. Aluminium and oxygen are present throughout the film, which indicates a complete ALD infilling. The aluminium and oxygen signals oscillate with a period of ~6.5 nm because the infilled void space is arranged in interconnected channels running along the $<100>_{SL}$ directions, parallel to the substrate surface (Supplementary Fig. 23). An SiO_2 interlayer (6 nm thick) and Al_2O_3 capping layer (8 nm thick) are also evident. Pb, Se and I are distributed homogeneously throughout the film. **c**, FTIR spectra of an epi-SL before and after alumina infilling and overcoating (20 nm of alumina). Infilling results in a strong bleach of the first exciton peak and the appearance of a 1S–1P intraband peak at ~0.2 eV. The spectrum of a 20 nm thick ALD alumina film (no QDs) is shown for reference. **d**, The output characteristics of a PbI_2-treated epi-SL FET before ALD infilling show substantial modulation of the source–drain current (I_D) by the gate bias (V_G). **e**, The output characteristics of an epi-SL transistor after infilling with amorphous alumina show the loss of gate modulation due to high doping. Supplementary Fig. 22 gives additional FET data and discussion.

free carrier concentrations low enough to be readily modulated with an applied gate bias (Fig. 5d and Supplementary Fig. 22). However, after ALD, the transistors became highly conductive and exhibited quasi-linear current–voltage curves with almost no modulation by the gate bias, due to a very high (nearly degenerate) free electron concentration (Fig. 5e and Supplementary Fig. 22). Strong doping by alumina infilling is remarkable because it has not been observed for amorphous PbSe QD films made using thiol, sulfide, thiocyanate or carboxylic acid ligands[7,46]. Apparently, specific aspects of the structure or surface chemistry of these EDA- and EDA/PbI_2-treated epi-SLs results in the formation of a high concentration of donor defects on alumina deposition. Although the origin of the excessive doping on ALD infilling is unclear at this time, our results underline the critical role of surface chemistry in determining the doping and electrical properties of QD epi-SLs. Careful control of surface chemistry will be essential in ongoing efforts to reduce energy disorder and trigger miniband formation in these materials.

We used dual-space structural analysis at the ensemble and single-grain levels to determine the complete unit cell of oleate-capped and epitaxial-fused PbSe QD SLs and the pathway of the oleate- to epi-SL transformation. We found that the attraction between the nearly ligand-free PbSe{100} facets produced a rhombohedrally distorted bcc oleate-capped SL in which each QD has six nearest neighbours with cofacial {100} facets. This remarkable structure enables epitaxial fusion of the {100} facets without the need for QD rotation and yields a highly ordered epi-SL with a distorted simple cubic unit cell. We show that the phase transition combines 3D collective epitaxy with atomic topotaxy of the QDs. This topo-epitaxial phase transition illustrates the multiscale spatial order that is possible with self-assembled QD solids. Knowledge of the formation mechanism provides a foundation for the rational fabrication of QD epi-SLs with improved spatial order and electrical properties. However, surface chemistry, not spatial order, may ultimately determine the electrical properties of such epi-SLs. We show that the carrier type and concentration change dramatically after infilling the films with alumina by ALD. Infilling has no effect on the SL structure but results in very high carrier densities. The development of well-defined, tunable and robust surface chemistries that minimize spatial and energetic disorder is essential to make QD epi-SLs that exhibit the emergent mesoscale property of delocalized band transport.

Online content

Any methods, additional references, Nature Research reporting summaries, source data, statements of code and data availability and associated accession codes are available at https://doi.org/10.1038/s41563-019-0485-2.

Received: 21 April 2019; Accepted: 15 August 2019;
Published online: 14 October 2019

References

1. Boles, M. A., Engel, M. & Talapin, D. V. Self-assembly of colloidal nanocrystals: from intricate structures to functional materials. *Chem. Rev.* **116**, 11220–11289 (2016).

2. Lazarenkova, O. L. & Balandin, A. A. Miniband formation in a quantum dot crystal. *J. Appl. Phys.* **89**, 5509–5515 (2001).
3. Jiang, C.-W. & Green, M. A. Silicon quantum dot superlattices: modeling of energy bands, densities of states, and mobilities for silicon tandem solar cell applications. *J. Appl. Phys.* **99**, 114902 (2006).
4. Whitham, K. et al. Charge transport and localization in atomically coherent quantum dot solids. *Nat. Mater.* **15**, 557–563 (2016).
5. Gómez-Campos, F. M., Rodríguez-Bolívar, S. & Califano, M. High-mobility toolkit for quantum dot films. *ACS Photon.* **3**, 2059–2067 (2016).
6. Guyot-Sionnest, P. Electrical transport in colloidal quantum dot films. *J. Phys. Chem. Lett.* **3**, 1169–1175 (2012).
7. Liu, Y. et al. PbSe quantum dot field-effect transistors with air-stable electron mobilities above $7\,cm^2\,V^{-1}\,s^{-1}$. *Nano Lett.* **13**, 1578–1587 (2013).
8. Kagan, C. R. & Murray, C. B. Charge transport in strongly coupled quantum dot solids. *Nat. Nanotechnol.* **10**, 1013–1026 (2015).
9. Evers, W. H. et al. High charge mobility in two-dimensional percolative networks of PbSe quantum dots connected by atomic bonds. *Nat. Commun.* **6**, 8195 (2015).
10. Evers, W. H. et al. Low-dimensional semiconductor superlattices formed by geometric control over nanocrystal attachment. *Nano Lett.* **13**, 2317–2323 (2013).
11. Baumgardner, W. J., Whitham, K. & Hanrath, T. Confined-but-connected quantum solids via controlled ligand displacement. *Nano Lett.* **13**, 3225–3231 (2013).
12. Dong, A., Chen, J., Vora, P. M., Kikkawa, J. M. & Murray, C. B. Binary nanocrystal superlattice membranes self-assembled at the liquid–air interface. *Nature* **466**, 474–477 (2010).
13. Dong, A., Jiao, Y. & Milliron, D. J. Electronically coupled nanocrystal superlattice films by in situ ligand exchange at the liquid–air interface. *ACS Nano* **7**, 10978–10984 (2013).
14. Sandeep, C. S. S. et al. Epitaxially connected PbSe quantum-dot films: controlled neck formation and optoelectronic properties. *ACS Nano* **8**, 11499–11511 (2014).
15. Boneschanscher, M. P. et al. Long-range orientation and atomic attachment of nanocrystals in 2D honeycomb superlattices. *Science* **344**, 1377–1380 (2014).
16. Zhao, M. et al. High hole mobility in long-range ordered 2D lead sulfide nanocrystal monolayer films. *Adv. Funct. Mater.* **26**, 5182–5188 (2016).
17. Geuchies, J. J. et al. In situ study of the formation mechanism of two-dimensional superlattices from PbSe nanocrystals. *Nat. Mater.* **15**, 1248–1254 (2016).
18. Walravens, W. et al. Chemically triggered formation of two-dimensional epitaxial quantum dot superlattices. *ACS Nano* **10**, 6861–6870 (2016).
19. Zhao, M. et al. Ligand effects on electronic and optoelectronic properties of two-dimensional PbS necking percolative superlattices. *Nano Res.* **10**, 1249–1257 (2017).
20. Treml, B. E. et al. Successive ionic layer absorption and reaction for postassembly control over inorganic interdot bonds in long-range ordered nanocrystal films. *ACS Appl. Mater. Interfaces* **9**, 13500–13507 (2017).
21. Balazs, D. M. et al. Electron mobility of $24\,cm^2\,V^{-1}\,s^{-1}$ in PbSe colloidal-quantum-dot superlattices. *Adv. Mater.* **30**, 1802265 (2018).
22. van Overbeek, C. et al. Interfacial self-assembly and oriented attachment in the family of PbX (X = S, Se, Te) nanocrystals. *J. Phys. Chem. C* **122**, 12464–12473 (2018).
23. Savitzky, B. H. et al. Propagation of structural disorder in epitaxially connected quantum dot solids from atomic to micron scale. *Nano Lett.* **16**, 5714–5718 (2016).
24. Whitham, K. & Hanrath, T. Formation of epitaxially connected quantum dot solids: nucleation and coherent phase transition. *J. Phys. Chem. Lett.* **8**, 2623–2628 (2017).
25. Peters, J. L. et al. Mono- and multilayer silicene-type honeycomb lattices by oriented attachment of PbSe nanocrystals: synthesis, structural characterization, and analysis of the disorder. *Chem. Mater.* **30**, 4831–4837 (2018).
26. Shannon, R. D. & Rossi, R. C. Definition of topotaxy. *Nature* **202**, 1000–1001 (1964).
27. Son, D. H., Hughes, S. M., Yin, Y. & Alivisatos, A. P. Cation exchange reactions in ionic nanocrystals. *Science* **306**, 1009–1012 (2004).
28. Macfarlane, R. J., Jones, M. R., Lee, B., Auyeung, E. & Mirkin, C. A. Topotactic interconversion of nanoparticle superlattices. *Science* **341**, 1222–1225 (2013).
29. Rossi, R. C. & Fulrath, R. M. Epitaxial growth of spinel by reaction in the solid state. *J. Am. Ceram. Soc.* **46**, 145 (1963).
30. Wang, Y. et al. Dynamic deformability of individual PbSe nanocrystals during superlattice phase transitions. *Sci. Adv.* **5**, eaaw5623 (2019).
31. Bealing, C. R., Baumgardner, W. J., Choi, J. J., Hanrath, T. & Hennig, R. G. Predicting nanocrystal shape through consideration of surface–ligand interactions. *ACS Nano* **6**, 2118–2127 (2012).
32. Ning, Z. et al. Air-stable n-type colloidal quantum dot solids. *Nat. Mater.* **13**, 822–828 (2014).
33. Brown, P. R. et al. Energy level modification in lead sulfide quantum dot thin films through ligand exchange. *ACS Nano* **8**, 5863–5872 (2014).
34. Harris, R. D. et al. Electronic processes within quantum dot–molecule complexes. *Chem. Rev.* **116**, 12865–12919 (2016).
35. Law, M. et al. Structural, optical, and electrical properties of PbSe nanocrystal solids treated thermally or with simple amines. *J. Am. Chem. Soc.* **130**, 5974–5985 (2008).
36. Anderson, N. C., Hendricks, M. P., Choi, J. J. & Owen, J. S. Ligand exchange and the stoichiometry of metal chalcogenide nanocrystals: spectroscopic observation of facile metal–carboxylate displacement and binding. *J. Am. Chem. Soc.* **135**, 18536–18548 (2013).
37. Choi, J. J. et al. Controlling nanocrystal superlattice symmetry and shape-anisotropic interactions through variable ligand surface coverage. *J. Am. Chem. Soc.* **133**, 3131–3138 (2011).
38. Weidman, M. C., Smilgies, D.-M. & Tisdale, W. A. Kinetics of the self-assembly of nanocrystal superlattices measured by real-time in situ X-ray scattering. *Nat. Mater.* **15**, 775–781 (2016).
39. Bian, K. et al. Shape-anisotropy driven symmetry transformations in nanocrystal superlattice polymorphs. *ACS Nano* **4**, 2815–2823 (2011).
40. Simon, P. et al. PbS–organic mesocrystals: the relationship between nanocrystal orientation and superlattice array. *Angew. Chem. Int. Ed.* **51**, 10776–10781 (2012).
41. Santra, P. K., Palmstrom, A. F., Tassone, C. J. & Bent, S. F. Molecular ligands control superlattice structure and crystallite orientation in colloidal quantum dot solids. *Chem. Mater.* **28**, 7072–7081 (2016).
42. Novák, J. et al. Site-specific ligand interactions favor the tetragonal distortion of PbS nanocrystal superlattices. *ACS Appl. Mater. Interfaces* **8**, 22526–22533 (2016).
43. Li, R., Bian, K., Hanrath, T., Bassett, W. A. & Wang, Z. Decoding the superlattice and interface structure of truncate PbS nanocrystal-assembled supercrystal and associated interaction forces. *J. Am. Chem. Soc.* **136**, 12047–12055 (2017).
44. Bian, K., Li, R. & Fan, H. Controlled self-assembly and tuning of large PbS nanoparticle supercrystals. *Chem. Mater.* **30**, 6788–6793 (2018).
45. Fan, Z. & Grünwald, M. Orientational order in self-assembled nanocrystal superlattices. *J. Am. Chem. Soc.* **141**, 1980–1988 (2019).
46. Liu, Y. et al. Robust, functional nanocrystal solids by infilling with atomic layer deposition. *Nano Lett.* **11**, 5349–5355 (2011).
47. Koh, W. K. et al. Heavily doped n-type PbSe and PbS nanocrystals using ground-state charge transfer from cobaltocene. *Sci. Rep.* **3**, 2004 (2013).
48. Araujo, J. J., Brozek, C. K., Kroupa, D. M. & Gamelin, D. R. Degenerately n-doped colloidal PbSe quantum dots: band assignments and electrostatic effects. *Nano Lett.* **18**, 3893–3900 (2018).

Acknowledgements

This work was supported by the UC Office of the President under the UC Laboratory Fees Research Program Collaborative Research and Training Award LFR-17-477148. We thank C. Zhu, E. Schaible and A. Liebman-Pelaez for training and assistance on Beamline 7.3.3 of the Advanced Light Source, T. Aoki for TEM assistance, Q. Lin for X-ray diffraction assistance and D. Smilgies for the use of his GISAXS software and useful correspondence. This research used resources of the Advanced Light Source, which is a DOE Office of Science User Facility under contract no. DE-AC02-05CH11231. Materials characterization was performed at the user facilities of the UC Irvine Materials Research Institute, which include instrumentation funded in part by the National Science Foundation Major Research Instrumentation Program under grant no. CHE-1338173.

Competing interests

The authors declare no competing interests.

Additional information

Supplementary information is available for this paper at https://doi.org/10.1038/s41563-019-0485-2.

Correspondence and requests for materials should be addressed to M.L.

Reprints and permissions information is available at www.nature.com/reprints.

Publisher's note Springer Nature remains neutral with regard to jurisdictional claims in published maps and institutional affiliations.

Methods

Materials. All the chemicals were used as received unless otherwise noted. PbO (99.999%), PbI_2, (99.9985%) and Se shot (99.999%) were purchased from Alfa Aesar. Oleic acid (OA, technical grade, 90%), diphenylphosphine (98%), 1-octadecene (90%), anhydrous EG (99.8%), anhydrous acetonitrile (99.99%), anhydrous hexanes (99%), anhydrous toluene (99.8%), anhydrous ethanol (99.5%), anhydrous tetrachloroethylene (TCE, 99%), 3-mercaptopropyltrimethoxysilane (95%), anhydrous carbon tetrachloride (>99.5%), ferrocene (>98%), trimethylaluminium (97%), ammonium thiocyanate (99.99%), 1,2-ethanedithiol (>98%) and anhydrous dimethyl sulfoxide (99.9%) were purchased from Sigma Aldrich. Anhydrous EDA (>98.0%) was purchased from TCI. Trioctylphosphine (technical grade, >90%) was acquired from Fluka and mixed with Se shot for 24 h to form a 1 M trioctylphosphine–Se stock solution. EG-d_4 (>99.9% CP, 99.3 atom% D) and EDA-d_4 (>99.9% CP, 99.3 atom% D) were purchased from Cambridge Isotope Laboratories. Toluene-d_8 (> 99% CP, 99.6 atom% D) was purchased from Sigma Aldrich and dried over 3 Å molecular sieves prior to use. Nitric acid (TraceMetal grade, Fisher Scientific) was distilled twice before use. The water used for substrate cleaning and ALD was 18.2 MΩ (Milli-Q Gradient). Water for ALD was degassed with three freeze–pump–thaw cycles before use.

QD synthesis. PbSe QDs were synthesized and purified using standard air-free techniques. PbO (1.50 g), OA (5.00 g) and 1-octadecene (10.00 g) were mixed and degassed in a three-neck round-bottom flask at room temperature. Then the mixture was heated at 110 °C under vacuum to form $Pb(OA)_2$ and dry the solution. After 1.5 h, the $Pb(OA)_2$ solution was heated to 180 °C under argon flow and 9.5 ml of a 1 M solution of trioctylphosphine–Se that contained 200 µl of diphenylphosphine was rapidly injected into this hot solution. An immediate darkening of the solution was observed, and the QDs were grown for 105 s at ~160 °C. The reaction was quenched with a liquid N_2 bath and injection of 10 ml of anhydrous hexanes. The QDs were purified in a N_2-filled glove box (<0.5 ppm O_2) by adding 10 ml of hexanes and 20 ml of ethanol to the reaction solution, collecting the QDs by centrifugation, performing one cycle of redispersion/precipitation using hexanes/ethanol (10 ml/20 ml) and then drying and storing the QDs as a powder in the glove box.

SL fabrication. SL fabrication was performed in N_2-filled glove boxes with <0.5 ppm O_2. Oleate-capped PbSe QD SLs were prepared by carefully drop casting 60–70 µl of a 6–10 mg ml^{-1} solution of PbSe QDs dispersed in hexanes onto 7 ml of EG in a Teflon well (3.5 cm wide × 5 cm long × 1 cm deep) that was cleaned by soaking overnight in 5 M nitric acid and then soaking and rinsing in Millipore water at least ten times. After depositing the QD solution, the well was immediately covered with a glass slide and the hexanes allowed to slowly evaporate in 6–8 min, which resulted in a smooth, dry QD film floating on the EG surface. The slide was then removed and 100 µl of a 7.5 M solution of EDA in acetonitrile was slowly (5–10 s) injected into the EG directly underneath the film. As the EDA solution spread throughout the well, the film visibly darkened, which indicated film densification and epi-SL formation. After 30 s, the darkened SL film nearest to the EDA injection point was transferred to a solid substrate (Si, glass or TEM grid) by manual stamping using a vacuum wand. All the substrates (except the TEM grids) were cleaned by 15 min of sonication in acetone, water and isopropanol, dried under flowing air, soaked in a 100 mM solution of 3-mercaptopropyltrimethoxysilane in toluene for 1 h to functionalize the surface for improved QD adhesion and then rinsed with neat toluene and dried under flowing air. The stamped film was rinsed vigorously with neat acetonitrile and dried under flowing N_2. Next, the SL film was immediately soaked in a 10 mM solution of PbI_2 in dimethyl sulfoxide for 5 min, rinsed with copious amounts of dimethyl sulfoxide and acetonitrile and dried under flowing N_2. Amorphous alumina deposition was performed in a homemade cold-wall travelling wave ALD system within a glove box using trimethylaluminium and water at a substrate temperature of 60 °C and a base pressure of 0.08 torr. Precursors were introduced to the ALD chamber using computer-controlled diaphragm valves in-line with a 130 sccm stream of N_2 carrier gas. Pulse and purge times were 20 ms and 75 s, respectively, for both precursors.

Basic characterization. Optical absorbance measurements of QDs dispersed in TCE were performed with a Perkin-Elmer Lambda 950 spectrophotometer. Neat TCE served as the background for the solution measurements. FTIR transmission spectra of SL films on double-side polished intrinsic Si substrates were acquired in dry air on a Nicolet 6700 spectrometer at a resolution of 4 cm^{-1} with a blank Si substrate as the background. SEM was performed on an FEI Magellan 400L XHR SEM operating at 10 kV and 25–50 pA. Samples for TEM-based EDS mapping were prepared on a Tescan GAIA3 SEM-FIB. X-ray photoelectron spectra were acquired with a Kratos AXIS Supra spectrometer using monochromatic Al Kα radiation at an X-ray power of 225 W. XPS samples were prepared on clean Si substrates soaked in 1% volume hydrofluoric acid solution for 10 min, rinsed with water and immediately (<2 min) transferred to a glove box (<0.5 ppm O_2). SL films deposited onto these substrates were transferred to the XPS system completely air-free via an integrated glove box. Oleate-capped SL spectra were charge corrected to place the aliphatic carbon of oleate at 284.6 eV, whereas the other spectra were charge corrected to align the Pb 4*f*5/2 peak of PbSe with that of the oleate-capped SL spectrum at 137.3 eV. ICP-MS measurements were carried out using the standard additions method on a Nu AttoM ES HR-ICP-MS spectrometer using 10 cycles of 500 sweeps with 500 µs dwells per peak. Samples were prepared by forming epi-SL films on the surface of EG inside a centrifuge tube, then vigorously mixing the entire solution and collecting the liquid by centrifugation through an Amicon Ultra-15 centrifugal filter unit (10 kDa molecular weight cutoff). The solutions were then diluted with 2% nitric acid before standards addition and measurement. A second set of ICP-MS experiments was completed by Huffman-Hazen Laboratories. For these experiments, samples were prepared by extracting the EG subphase from beneath epi-SL films after a typical treatment time (30–45 s) and then filtering out any residual QDs using an Amicon Ultra-15 filter. Additional details about the ICP-MS experiments are provided in Supplementary Method 2.

Isotope labelling experiments. For tests with EG-d_4, SL films were prepared as described above on the surface of EG-d_4 in smaller, circular Teflon wells (~1 ml of EG-d_4). An aliquot of 20 µl of 7.5 M EDA in acetonitrile was injected to achieve the same overall concentration as in the larger wells (~105 mM) and allowed to react for 30 s. Films were stamped onto double-side polished Si and measured by FTIR spectroscopy. For tests with EDA-d_4, a 1:1 volume mixture of EDA-d_4 and acetonitrile was injected into the EG subphase of the normal wells and allowed to react for 3–8 min before stamping the films onto double-side polished Si for the FTIR measurements. Attenuated total reflectance FTIR spectra of neat EG, EG-d_4, EDA and EDA-d_4 were collected as references.

Determination of oleate surface coverage. The oleate/QD ratio and oleate surface coverage (oleate nm^{-2}) were determined using NMR spectroscopy and optical absorbance spectroscopy following a modified version of a published procedure[49]. Known masses of dried QDs from syntheses with two, three or four cleaning cycles (one cycle consists of redispersion with 20 ml of hexane followed by precipitation with 10 ml of ethanol) were dispersed in anhydrous toluene-d_8 (dried over molecular sieves) and injected into precision NMR tubes (Wilmad, 528-PP-7). ^{1}H NMR spectra were acquired at 296 K with a Bruker DRX 500 spectrometer (500 MHz, BBO probe) using 16 scans at a delay time of 100 s to accommodate the long T_1 relaxation times of surface-bound oleate. The absolute concentration of the oleate ligands was determined with an internal reference (6.45 mM of ferrocene). The QD number concentration was determined from optical absorption spectra of QD suspensions using the size-dependent molar extinction coefficient of Moreels et al.[49]. An aliquot of 51 µl of the QD suspension used for NMR was removed prior to ferrocene addition, dried under nitrogen flow and vacuum, and redispersed in a known volume of TCE. The absorbance of this suspension at $h\nu = 3.1$ eV was measured, background corrected against neat TCE and used to calculate the QD number concentration using $c = \frac{A_{3.1\,eV}}{0.0277(ld^3)}$, where c is the QD concentration (µM), $A_{3.1\,eV}$ is the absorbance at a photon energy of 3.1 eV, l is the path length (cm) and d is the QD diameter (nm)[49]. We note that although this equation was derived specifically for PbSe QDs suspended in CCl_4, the use of TCE as the solvent gave the same absorbance values to within ±1%. The oleate/QD ratio was then calculated from the measured oleate and QD concentrations. The average oleate coverage (oleate nm^{-2}) was calculated by dividing the oleate/QD ratio by the surface area per QD (145 nm^2) from our STEM-derived structural model of these QDs[30]. Supplementary Information gives details on the error analysis and our estimates of oleate coverage on the {100}, {110} and {111} facets of the QDs.

Small-angle X-ray scattering. GISAXS and solution transmission SAXS measurements were performed on Beamline 7.3.3 of the Advanced Light Source at Lawrence Berkeley National Laboratory using 10 keV monochromatic X-rays ($\lambda = 1.24$ Å) with an energy bandwidth of 1%. For GISAXS measurements, the SL films were prepared on Si substrates and transported with the QD suspensions under nitrogen to minimize air exposure prior to measurement. However, measurements were performed in air. A Dectris Pilatus 2M detector with a pixel size of 0.172 × 0.172 mm and 1,475 × 1,679 pixels was used to record the 2D scattering patterns. A silver behenate standard was used to determine the sample-to-detector distance and beam centre. Exposure times ranged from 0.2 to 30 s. The grazing angle of incidence was varied from 0.2° to 0.3°. Manual pattern fitting was performed using the IndexGIXS software package provided by Detlef Smilgies of the Cornell High Energy Synchrotron Source. The critical angles of the films were fitted empirically (0.195° for the oleate-capped SLs and 0.21° for the epi-SLs) to capture the breadth of the Yoneda band. For solution SAXS measurements, a 30 mg ml^{-1} octane suspension of QDs was drawn into a 2 × 0.2 mm glass capillary with a 0.150 mm wall thickness (Electron Microscopy Sciences). The solution was exposed to air briefly before and during measurement. The sample-to-detector distance was 2,994.78 mm as calibrated by the silver behenate standard. The signal was collected for 120 s, and an octane-filled blank capillary was used for background subtraction. The Nika software package[50] in Igor Pro was used to azimuthally integrate (25–75°) the SAXS pattern and corrected for the background using the octane-filled blank. Particle distribution fitting was performed using a spherical form factor with a Gaussian spread of QD diameters in the NIST SANS Analysis package in Igor Pro[51]. No instrumental broadening was included in the fitting procedure, which indicates the reported polydispersity is probably an overestimation.

TEM. A JEOL JEM-2100F TEM operated at 200 kV was used to image isolated QDs prepared by drop casting ~2 µl of a dilute (<1 mg ml^{-1}) hexane suspension onto a lacey carbon grid (with a carbon film). SL samples for TEM analysis were prepared by stamping QD films from the EG surface onto holey carbon TEM grids (without a carbon film coating). The use of TEM grids free of a carbon film was critical for high-quality SEI in the TEM. Imaging, diffraction and EDS elemental mapping were performed on a JEOL JEM-2800 TEM. STEM experiments (SEI and EDS mapping) employed a probe size of 1.0 nm. Hyperspectral EDS images were collected using a 30 min acquisition time. Electron diffraction patterns were acquired at a parallel beam condition. The sample holder tilt was 0° unless otherwise noted. Correlated SEI and SAED experiments were carried out by first imaging a SL grain in STEM mode with the secondary electron detector and then switching to the TEM mode to collect the SAED pattern of the same location. The image rotation between STEM, diffraction and imaging modes was corrected for in our correlated S/TEM experiments to yield a rotational alignment error of <5°.

Electrical measurements. All FET measurements were performed at room temperature in a glove box at a sweep rate of ~40 V s^{-1} using a Keithley 2636B source measure unit run by custom LabView software. The transistors were fabricated in a bottom contact (5 nm Ti, 35 nm Au), global back gate (p^{++} Si, 200 nm SiO_2, $C_{ox} = 17.5$ nF cm^{-2}) geometry with a channel length and width of $L = 25$ µm and $W = 1{,}000$ µm, respectively. Linear field-effect mobilities (μ_{lin}) were determined at source–drain bias $|V_{SD}| = 10$ V and absolute gate bias $|V_G| = 40$ V using the gradual channel approximation equation for electron and hole mobility:

$$\left.\frac{dI_D}{dV_G}\right|_{V_{SD}} = \frac{WC_{ox}V_{SD}}{L}\mu_{lin}$$

Data availability

The datasets generated and/or analysed during the current study are available from the corresponding author on reasonable request.

References

49. Moreels, I. et al. Composition and size-dependent extinction coefficient of colloidal PbSe quantum dots. *Chem. Mater.* **19**, 6101–6106 (2007).
50. Ilavsky, J. Nika: software for two-dimensional data reduction. *J. Appl. Cryst.* **45**, 324–328 (2012).
51. Kline, S. R. Reduction and analysis of SANS and USANS data using IGOR Pro. *J. Appl. Cryst.* **39**, 895–900 (2006).